Electron-phonon and electron-photon interactions and resonant Raman scattering from the radial-breathing mode of single-walled carbon nanotubes

Valentin N. Popov,* Luc Henrard, and Philippe Lambin
Laboratoire de Physique du Solide, Facultés Universitaires Notre-Dame de la Paix, Rue de Bruxelles 61, B-5000 Namur, Belgium
(Received 24 January 2005; revised manuscript received 1 April 2005; published 14 July 2005)

The resonance Raman profile of the radial-breathing mode is calculated for all 300 single-walled carbon nanotubes in the radius range from 2 Å to 12 Å and for all optical transitions up to 3.5 eV using a symmetry-adapted nonorthogonal tight-binding model [V. N. Popov, New J. Phys. **6**, 17 (2004)]. The influence of the electron-phonon and electron-photon interactions on the Raman intensity is studied using an approximate expression for the intensity in the vicinity of each optical transition as the product of the electron-phonon coupling matrix element, the momentum matrix element, and the effective mass raised to different powers. The dependence of the latter three quantities and the maximum Raman intensity on the nanotube radius, the chiral angle, and the optical transition energy is discussed in detail. In particular, the points of the corresponding plots exhibit family behavior of three different types. It is shown that the widespread practice to neglect the electron-photon and electron-phonon interactions in the estimation of the intensity can lead to incorrect prediction of the Raman spectra.

DOI: 10.1103/PhysRevB.72.035436 PACS number(s): 73.63.Fg, 63.22.+m, 78.30.Na

I. INTRODUCTION

Carbon nanotubes have unusual vibrational, electronic, and optical properties due to their quasi-one-dimensionality.[1] The synthesized nanotubes consist either of a single graphitic layer [single-walled nanotubes (SWNTs)] or a number of coaxial layers [multiwalled nanotubes (MWNTs)]. The nanotubes are observed quite often in bundles of many tubes. The low-frequency vibrational mode in the nanotubes with uniform radial atomic displacements [the radial-breathing mode (RBM)] gives rise to a high-intensity Raman line that can be used for the structural characterization of the samples by means of Raman spectroscopy. The frequency of the RBM, calculated within force constant models,[2,3] was found to be inversely proportional to the nanotube radius. The calculations within the density-functional approach using the local-density approximation (LDA) showed a slight dependence of this frequency on the nanotube chirality.[4,5] The interactions between the separate nanotubes in a bundle or between the layers in a MWNT modify the frequencies of the RBMs of the isolated nanotubes.[6,7]

The Raman scattering from nanotubes has the remarkable peculiarity that it takes place mainly under resonant conditions.[1] This means that the Raman spectra show distinct features due to certain nanotubes only when the laser excitation energy comes close to the optical transitions of these tubes. For this reason, the Raman spectrum measured at a given laser energy consists of a small number of lines compared to the otherwise large number of different nanotubes present in the sample. The optical transitions of SWNTs, calculated within the π-band tight-binding model (πTB model),[8] orthogonal and non orthogonal tight-binding models,[9,10] and the LDA approach,[11] underestimate the observed absorption and emission energies. This disagreement is mainly due to the neglect of the self-energy and excitonic effects on the band energies.[12] In a recent analysis of the electron interactions in nanotubes,[13] it was argued that the one-dimensional (1D) interaction and excitonic effects compete and nearly cancel. The remaining two-dimensional (2D) (graphene) interactions were found to lead to a logarithmic correction to the band energies that can explain fairly well the difference between the observed optical transitions and the predictions of the noninteracting models above.

The experimental Raman data have been so far assigned using mostly the predictions of force-constant models for the RBM frequency and the optical transition energies of the πTB model.[1] Recent well-resolved spectrofluorimetric data from HiPCO samples[14] allowed the derivation of empirical expressions for the transition energies of narrow semiconducting tubes.[15] The low-frequency Raman spectra of high-pressure CO (HiPCO) samples[16] were assigned using these empirical expressions and an empirical formula for the radius dependence of the frequency of the RBM. Recently, similar relations have been derived from the analysis of extensive Raman data obtained using tunable laser sources[17,18] Such empirical relations can be applied to determine accurately the Raman shift of the lines corresponding to the RBM frequencies of certain tubes and the laser energies that are favorable for the observation of these lines. However, the Raman lines originating from different tubes can have different maximum intensity, varying from very low to very high, which makes the Raman spectra assignment a challenge. Therefore, for the unambiguous determination of the radius and chirality distribution of the tubes in the sample, one has to know the dependence of the Raman line intensity on the laser energy [the so-called resonance Raman profile (RRP)]. So far, most of the quantum-mechanical simulations of the RRP have used the πTB electronic band structure of the nanotubes and have considered the momentum and electron-phonon coupling matrix elements as tube-independent.[19,20] In a few cases, the momentum matrix elements were calculated within more sophisticated models and the electron-phonon matrix elements were assumed to be equal to the first derivative of the transition energy with respect to the nanotube

radius.[21,22] To the best of our knowledge, no results for the RRP within the excitonic picture have been published so far. Recently, we have reported the results of the calculations of the RRP for 50 narrow semiconducting nanotubes carried out within a well-tuned nonorthogonal tight-binding model,[23] showing in particular that the maximum Raman intensity can vary from very low to very high for different tubes. These RRPs were used to simulate the Raman spectra of SWNT samples and a fair agreement was reached with available Raman data on HiPCO samples.[16]

In this paper, we propose a systematic study of the tube-dependent behavior of the maximum Raman intensity with respect to the strength of the electron-photon and electron-phonon interactions. First, we present the maximum Raman intensities calculated within a symmetry-adapted nonorthogonal tight-binding model[9,10] for all 300 nanotubes in the radius range from 2 Å to 12 Å, which contains practically all nanotubes currently produced by various techniques. Next, in the analysis of the Raman intensity, we used an approximate expression that is proportional to the product of the electron-phonon coupling and momentum matrix elements, and the electron effective mass raised to different powers. We calculated the dependence of the latter three quantities on the nanotube radius, chiral angle, and transition energy and discussed the effect of the interactions of the electrons with photons and phonons, and of the electronic band structure of the nanotubes on the maximum Raman intensity. We observed three different types of family patterns for the latter quantities. The dependence of the optical absorption coefficient on the structural properties of the nanotubes is also calculated. The results for the maximum Raman intensity and the absorption coefficient are used in the discussion of the conditions for the observation of the different nanotube types using Raman scattering spectroscopy and optical absorption spectroscopy. The paper ends with conclusions.

II. THEORETICAL PART

The nanotube can be considered as being obtained by the rolling up of an infinite strip of graphene along the chiral vector $\mathbf{C}_h = L_1\mathbf{a}_1 + L_2\mathbf{a}_2$ ($\mathbf{a}_1$ and $\mathbf{a}_2$ are the primitive translations of graphene) into a seamless cylinder. The integer numbers L_1 and L_2 ($L_1 \geqslant L_2 \geqslant 0$) specify uniquely the nanotube. There are "armchair" tubes ($L_1 = L_2$), "zigzag" tubes ($L_1 \neq L_2 = 0$), and chiral tubes (all the rest). The nanotube can be characterized by its radius R and chiral angle θ, which is the angle between the chiral vector and the nearest zigzag of carbon-carbon bonds. All nanotubes possess a screw symmetry defined by two different primitive screw operations. Choosing the same two-atom unit cell as for graphene, any other unit cell of the tube can be obtained by a suitable combination of integer numbers times these two operations. The incorporation of the screw symmetry in the calculations of various properties of nanotubes leads to drastic reduction of the computational time.[3]

Recently, we have implemented a symmetry-adapted nonorthogonal tight-binding model (NTB model) in the calculations of the band structure and the dielectric function of practically all existing carbon nanotubes.[9,10] In the NTB model, the electronic band structure of a nanotube is obtained by solving the matrix eigenvalue equation[9]

$$\sum_{r'} (H_{klrr'} - E_{kl} S_{klrr'}) c_{klr'} = 0. \tag{1}$$

Here $H_{klrr'}$ and $S_{klrr'}$ are the matrix elements of the Hamiltonian and the overlap matrix elements, respectively, E_{kl} is the one-electron eigenenergy, and $c_{klr'}$ are the coefficients in the expansion of the one-electron wave function as a linear combination of the atomic orbitals of the two-atom unit cell. The one-dimensional wave vector k and the integer quantum number l are consequences of the translational and the rotational symmetries of the nanotubes ($-\pi \leqslant k \leqslant \pi$, $-N_c/2 < l \leqslant N_c/2$; N_c is the number of carbon pairs in the translational unit cell). The index r labels the $2n$ atomic orbitals of the two-atom unit cell ($n=1$ for the π-band tight-binding model and $n=4$ for the all-valence tight-binding model using $2s$, $2p_x$, $2p_y$, and $2p_z$ orbitals for carbon). The eigenvalue equation, Eq. (1), yields the one-electron eigenenergies E_{klm} and the expansion coefficients c_{klmr}, $m = 1, 2, \ldots, 2n$. For each k, this equation has to be solved for all values of l, i.e., N_c times. Therefore, the computational time for solving the eigenvalue problem for each k using standard diagonalization techniques scales as $(2n)^3 N_c$ in the symmetry-adapted scheme and as $(2nN_c)^3$ in any non-symmetry-adapted scheme. The advantage of the former is obvious and it makes possible large-scale calculations of the Raman intensity of nanotubes where a sampling of a large number of wave vectors is required for the numerical integration over the one-dimensional Brillouin zone of the nanotube.

The Raman-scattering process can be described quantum mechanically considering the system of the electrons and phonons of the tube and the photons of the electromagnetic radiation and their interactions.[24] The most resonant Stokes process includes (a) absorption of a photon (energy E_L, polarization vector $\boldsymbol{\epsilon}^L$) with excitation of the electronic subsystem from the ground state with creation of an electron-hole pair, (b) scattering of the electron (hole) by a phonon (frequency ω_o, polarization vector $\mathbf{e}$), and (c) annihilation of the electron-hole pair with emission of a photon (energy $E_S = E_L - \hbar\omega_o$, polarization vector $\boldsymbol{\epsilon}^S$) and return of the electronic subsystem to the ground state. The Raman intensity for the Stokes process per unit tube length is given by

$$I(E_L, \omega_o) = A \left| \frac{1}{L} \sum_{cv} \frac{p_{cv}^S D_{cv} p_{cv}^{L*}}{(E_L - E_{cv} - i\gamma_{cv})\,(E_S - E_{cv} - i\gamma_{cv})} \right|^2, \tag{2}$$

where $A = C\,(E_S^2/E_L^2)\,(n+1)$, C is a constant, n is the phonon Bose-Einstein factor, and L is the length of the tube containing N unit cells. E_{cv} is the vertical separation between two states in the valence band $v \equiv klm$ and the conduction band $c \equiv kl'm'$, and γ_{cv} is the excited state width. $p_{cv}^{L,S}$ is the matrix element of the component of the momentum in the direction of the polarization vector $\boldsymbol{\epsilon}^{L,S}$. The electron-phonon coupling matrix element D_{cv} is determined by the scalar product of the derivative of E_{cv} with respect to the atomic displacement vector $\mathbf{u}$ and the phonon eigenvector $\mathbf{e}$

$$D_{cv} = \sqrt{\frac{\hbar}{2M\omega_o}} \sum_{i\gamma} e_{i\gamma} \frac{\partial E_{cv}}{\partial u_{i\gamma}}. \quad (3)$$

Here, M is the mass of the carbon atom and $u_{i\gamma}$ is the γ component of the displacement of the ith atom in the two-atom unit cell. The radial-breathing mode is an almost uniform radial motion of the tube with negligible nonradial components of the atomic displacements, even for very-small-radius tubes. Assuming uniform radial deformation of the tube, it is readily seen that $\Sigma_{i\gamma} e_{i\gamma} (\partial E_{cv}/\partial u_{i\gamma})$ is proportional to the derivative of E_{cv} with respect to the tube radius. The derivatives with respect to the atomic displacements or the tube radius can be estimated using the Hellmann-Feynman theorem.

The analysis and the application of the obtained RRPs are facilitated by the use of a convenient approximate expression of the RRPs. As it will be shown in the next section, the features of the RRPs, arising from the optical transitions with energies E_{ii} ($ii=11,22,\ldots$ for the first, second, etc., optical transition), are well separated and nonoverlapping in most cases. This fact allows approximating each feature independently of the other features of a given profile. The most suitable function can be obtained from the estimation of the Raman intensity assuming two approximations. First, the points of the Brillouin zone corresponding to the spikes of the electronic density of states (the so-called van Hove singularities) will give predominant contribution to the sum in Eq. (2). Therefore, the numerator in the right-hand side can be assumed as k independent and can be pulled out of the summation at the wave vector k_{ii} of the optical transition E_{ii}. Second, the remaining summation can be performed as an analytical integration over the Brillouin zone of the tube for a particular optical transition[22] replacing the sum over k with $(L/2\pi)\int dk$ and using the effective-mass approximation. Namely, in the vicinity of the optical transition E_{ii}, the difference between the energies of the valence and conduction bands can be written as $E_{cv}=E_{ii}+\hbar^2(k-k_{ii})^2/2m_{ii}^*$, where m_{ii}^* is the effective mass of the transition. As a result, the integral over k is transformed into an integral over the energy: $(L/2\pi\hbar)\sqrt{m_{ii}^*/2}\int dE/\sqrt{E-E_{ii}}$. The summation in Eq. (2) then yields

$$\int \frac{1}{(E_L - E - i\gamma_{cv})(E_S - E - i\gamma_{cv})} \frac{dE}{\sqrt{E-E_{ii}}} = \frac{i\pi}{\hbar\omega} \left(\frac{1}{\sqrt{E_L - E_{ii} - i\gamma_{cv}}} - \frac{1}{\sqrt{E_S - E_{ii} - i\gamma_{cv}}} \right). \quad (4)$$

The electronic response is strongly suppressed for incident and scattered light polarizations perpendicular to the tube axis and is largest for polarizations parallel to the tube axis. For the intermediate cases, the Raman intensity is determined by the component of the polarization vectors along the tube and, therefore, will be proportional to $(\cos\varphi)^4$ where φ is the angle between the polarization vectors and the tube axis.[23] Then, we can restrict ourselves to light polarizations parallel to the tube axis (z axis) and obtain the approximating function for the feature of the RRP at the transition energy E_{ii} in the form

$$I_{ii}(E_L,\omega_o) = A' |p_{ii}|^4 D_{ii}^2 m_{ii}^* |F_{ii}|^2. \quad (5)$$

Here

$$F_{ii} = \frac{2}{\hbar\omega_o} \left(\frac{1}{\sqrt{E_L - E_{ii} - i\gamma_{cv}}} - \frac{1}{\sqrt{E_S - E_{ii} - i\gamma_{cv}}} \right) \quad (6)$$

and $A'=C'\ (E_S^2/E_L^2)\ (n+1)$, C' is a constant, p_{ii} is the matrix element of the z component of the momentum, and D_{ii} is the electron-phonon coupling matrix element evaluated at the optical transition E_{ii}.

The Raman intensity, as approximated by Eq. (5), is a symmetric function of the laser energy with respect to $E_L=E_{ii}+\hbar\omega_o/2$ (see Refs. 22 and 23). For small γ_{cv}, it has two peaks corresponding to the two resonances at $E_L=E_{ii}$ and $E_L=E_{ii}+\hbar\omega_o$. For the experimentally measured values of γ_{cv}, the two peaks merge into a single bell-like peak with a maximum at $E_L=E_{ii}+\hbar\omega_o/2$. We are going to consider only the latter case. The width of the approximating function depends on the optical transitions E_{ii} and the phonon frequency ω_o, both of which are available either as results of calculations or as empirical relations. The width of this function also depends on the excited state width γ_{cv}, which arises from the not yet well-studied processes of relaxation of the electronic excitations in nanotubes and is usually assumed to be a tube-independent parameter.

It is convenient to rewrite Eq. (5) in the form

$$I_{ii}(E_L,\omega_o) = A' I_{1,ii}^m \left| \frac{F_{ii}}{F_{ii}^m} \right|^2, \quad (7)$$

where F_{ii}^m is the value of F_{ii} at $E_L=E_{ii}+\hbar\omega_o/2$. The quantity $I_{1,ii}^m$ is equal to the maximum of $I_{ii}(E_L,\omega_o)$ (up to the factor A') and will be referred to as the maximum Raman intensity. It is given by the expression

$$I_{1,ii}^m = |p_{ii}|^4 D_{ii}^2 m_{ii}^* |F_{ii}^m|^2. \quad (8)$$

The index 1 is added to designate that this quantity is an approximation to the maximum Raman intensity of the full calculation [Eq. (2)].

Most of the empirical models of the band structure use constant parameters and therefore the derivatives of the band energy with respect to the atomic coordinates as well as the intensity are zero. In the *ab initio* approach, both p_{ii} and D_{ii} can be derived, but this is accompanied with increasing computational difficulties. However, the effective masses m_{ii}^* can be easily calculated within all models from the electronic band structure of the tubes. Then, it is tempting to assume p_{ii} and D_{ii} as tube-independent constants and use as "zeroth-order" approximation the simpler expression for the the peak intensities

$$I_{0,ii}^m = C'' m_{ii}^* |F_{ii}^m|^2, \quad (9)$$

where C'' is a constant.

In some cases, more than one pair of valence and conduction bands contributes to a given optical transition and the maximum intensity given by Eqs. (8) and (9) has to be corrected. In armchair and zigzag tubes, the bands with quantum numbers $\pm l$ ($l\neq 0, N_c/2$) are degenerate and, for the corresponding transitions, the maximum intensity must be multi-

plied by 4. The transitions in the armchair and the majority of the transitions in chiral tubes take place inside the Brillouin zone at points $\pm k_{ii}$ and, for these transitions, the maximum intensity must be multiplied by 4. Finally, there is a degeneracy of all bands with respect to electron spin, which gives rise to the same multiplicative factor for all optical transitions.

The presentation of the features of the RRP in the form of Eq. (7) is very convenient for the analysis of the resonant Raman intensity. Indeed, the expression in the right-hand side of this equation is the product of a tube-dependent parameter $A' I^m_{1,ii}$ and a bell-like function of E_L equal to 1 for $E_L = E_{ii} + \hbar\omega_o/2$. The former characterizes the maximum Raman intensity and the latter determines the shape of the RRP. In the next section, we shall consider in more detail the dependence of the parameters $I^m_{1,ii}$ on the tube radius, chirality, and transition energies through the constituent matrix elements of the electron-phonon coupling and the momentum, as well as the effective mass.

The nanotube samples can also be characterized by means of optical absorption spectroscopy. An approximate expression of the maximum absorption coefficient at the optical transitions can be derived assuming independent contributions of the separate optical transitions. Considering p_{cv} as k independent, it can be pulled out of the sum over the wave vector in the expression for the imaginary part of the dielectric function.[9] The latter sum can be transformed into an integral and evaluated within the effective-mass approximation to obtain the maximum absorption coefficient $\alpha^m_{1,ii}$ at the transition energy E_{ii} up to a constant multiplier as

$$\alpha^m_{1,ii} = \frac{1}{E_{ii}} |p_{ii}|^2 \sqrt{m^*_{ii}}. \tag{10}$$

In this case, the "zeroth-order" approximation would be to assume the matrix elements of the momentum to be constants and write the absorption coefficient as $\alpha^m_{0,ii} = C''' \sqrt{m^*_{ii}}/E_{ii}$ (C''' is a constant). The presence of degenerate bands and transitions inside the Brillouin zone will require correction factors of 2 in Eq. (10). The results of the calculations obtained using Eqs. (8) and (10) can be the basis for comparison of the conditions for observation of nanotubes by Raman and absorption spectroscopies.

III. RESULTS AND DISCUSSION

A. Resonance Raman profiles

We used Eq. (2) to calculate the RRP for the relaxed structure of all 300 semiconducting and metallic nanotubes in the radius range 2 Å $< R <$ 12 Å and for optical transitions $E_{ii} < 3.5$ eV within the NTB model.[9] This model does not include self-energy corrections and the obtained E_{ii} underestimate the experimental data[14] by about 0.3 eV.[10] Since the radius and chirality dependence of this correction is not known, throughout the paper we use the uncorrected NTB values of E_{ii}. We restricted ourselves to incident and scattered light polarizations parallel to the tube axis, for which only electronic transitions $klm \rightarrow klm'$ are dipole-allowed.[23] For the RBM frequency ω_o, the empirical formula[15] $\omega_o = 1117.5/R + 12.5$ was used (ω_o is in cm^{-1} and R is the radius of the nonrelaxed tube in Å for nearest carbon-carbon separation $a_{C\text{-}C} = 1.44$ Å). The excited-state width was taken to be $\gamma_{cv} = 0.03$ eV, which is consistent with recent experimental data.[16,22] The summation in Eq. (2) was performed over $5000/\sqrt{N_c}$ k points in the Brillouin zone, which were found to be enough for the convergence of the sum.

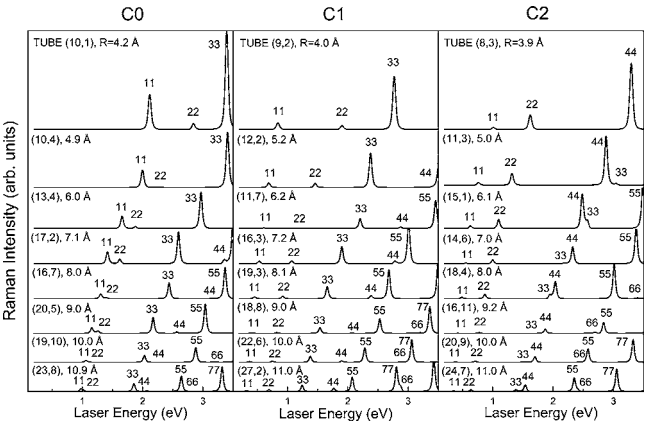

FIG. 1. The calculated RRPs of 24 SWNTs belonging to the groups $C0$, $C1$, and $C2$. The labeling of the optical transitions ii follows that of the πTB model in the linear dispersion approximation. The intensity is in arbitrary units and the scale is the same in all graphs.

The obtained RRPs have a different behavior for nanotubes with residual $\nu = 0$, 1, or 2 of the division of $L_1 - L_2$ by 3. For this reason, we consider these three cases separately and adopt the notation $Z0$, $Z1$, and $Z2$ for zigzag tubes, and $C0$, $C1$, and $C2$ for chiral tubes. Armchair tubes are denoted here with A. In Fig. 1, the calculated RRPs for 24 tubes belonging to groups $C0$, $C1$, and $C2$ are shown. It is seen that the maximum intensity I^m_{ii} increases with the increase of the transition energy and decreases with the increase of the radius. Apart from these general trends, I^m_{ii} depends on the index ii of the optical transition.

Before continuing with this specific dependence, we note that the transition energies of the nanotubes can be estimated simply from the appropriately folded πTB band structure obtained assuming linear dispersion close to the K and K' points in the Brillouin zone of graphene. The resulting expression $E^0_{ii} = i\gamma_0 a_{C\text{-}C}/R$ (γ_0 is the hopping integral) gives for $i = 1, 2, 4, 5, \ldots$ the transition energies with $ii = 11, 22, 33, 44, \ldots$ in tubes $C1$, $C2$, $Z1$, and $Z2$, and for $i = 3, 6, \ldots$ the transition energies with $ii = 11, 22, \ldots$ in tubes $C0$, A, and $Z0$. The trigonal warping effect[1] gives rise to a shift of the energies for tubes $C1$, $C2$, $Z1$, and $Z2$ to new values E_{ii} and a splitting of the energies for tubes $C0$ and $Z0$ into two components: $E^0_{11} \rightarrow (E_{11}, E_{22}), E^0_{22} \rightarrow (E_{33}, E_{44}), \ldots$. Because of the shift and the splitting of the transition energies, the $1/R$ curves will widen into strips with the points for zigzag tubes lying on the boundaries and the points for the chiral and armchair tubes lying inside the strips. Although the order of E_{ii} can be different from that of E^0_{ii}, we did not relabel the former. This explains why for some of the RRPs in Fig. 1, we have, e.g., $E_{66} > E_{77}$ (central panel) and $E_{55} > E_{66}$ (right panel).

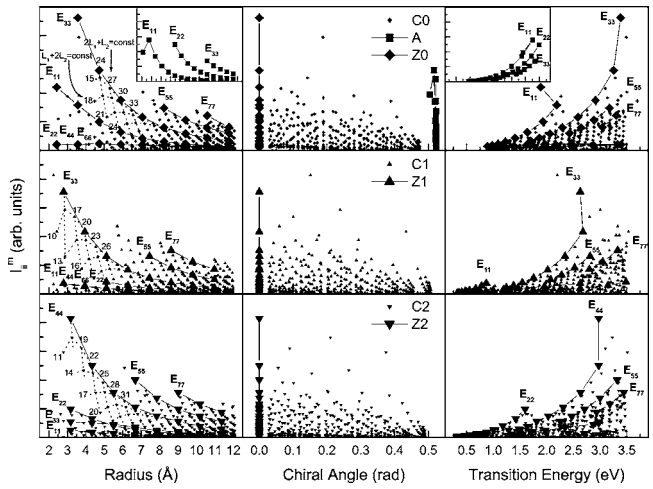

FIG. 2. The calculated maximum Raman intensity I_{ii}^m of the RBM for all optical transitions up to 3.5 eV and for all 300 SWNTs in the radius range 2 Å$<R<$12 Å versus the tube radius, the chiral the angle, and the transition energy. The data for the groups $(C0,A,Z0)$, $(C1,Z1)$, and $(C2,Z2)$ are presented in separate panels. I_{ii}^m is given in arbitrary units and the scale is the same for all graphs. The points for the armchair and zigzag groups are connected by solid lines. The points following two different family patterns are connected by dotted lines. The numbers are the values of L_1+2L_2 or $2L_1+L_2$.

In Fig. 1, the peak positions of the RRPs close to the transition energies $(E_{11},E_{22}),(E_{33},E_{44}),\ldots$ in tubes $C0$ and $E_{11},E_{22},E_{33},\ldots$ in tubes $C1$ and $C2$ versus radius lie on strips similar to the strips on the transition energy-radius plot mentioned above. The maximum intensity I_{ii}^m is larger for transitions 11, 33,55, 77, … in tubes $C0$, transitions 33, 55,77, … in tubes $C1$, and transitions 22, 44,55, 77,…in tubes $C2$ (we will use the notation C_H for the set of these transitions) than for the rest of the transitions in tubes $C0$, $C1$, and $C2$ (set C_L). Similar behavior is observed for zigzag tubes where the transitions can be grouped in two sets Z_H and Z_L as well. The predicted behavior for tubes $C0$ and $Z0$ corresponds to the experimental observation of much higher intensity for the lower-energy component of each of the pairs $(E_{11},E_{22}),(E_{33},E_{44}),\ldots$.[17,18] The results for semiconducting tubes agree with the observed much stronger Raman signal from the E_{22} transitions in tubes $C2$ and $Z2$ than in tubes $C1$ and $Z1$.[18]

The dependence of the maximum Raman intensity I_{ii}^m on the radius, the chiral angle, and the transition energy is shown for all studied tubes in Fig. 2. As it can be seen in the left panels, the points for a given transition ii form striplike patterns and have two types of family behavior for nanotubes with $L_1+2L_2=3\mu+\nu$ and $2L_1+L_2=3\mu+\nu$ (μ is an integer number). The family behavior of the intensity-radius plots can be used similarly to that of the energy-radius plots for the analysis of the experimental Raman data. For each ii, I_{ii}^m decreases with the increase of the radius and tends to zero for the radius tending to infinity. For a nanotube sample with a certain radius distribution, the tubes and transitions of set C_H will have larger maximum intensity than those of set C_L and, for each transition, the zigzag tubes will give rise to largest maximum intensity. The points for transitions 11, 22,33, … in armchair tubes have values close to those for transitions 11, 33,55, … in tubes $Z0$ (see inset of Fig. 2). Note that points for tubes with close radii normally correspond to transitions with different transition energies.

In Raman-scattering experiments, the samples are probed with a given laser excitation energy, and therefore, it is important to display the intensity against the transition energy as well. The plots in the right panels of Fig. 2 reveal that, for each ii, I_{ii}^m increases with the increase of the energy and that the points follow the same two types of family patterns as in the left panels (not shown). Again, similarly to the left panels, the points of set C_H have larger maximum intensity than those of set C_L. The points with close energies generally correspond to tubes with different radii. For the quantitative analysis of the Raman spectra of a sample at a given laser energy, one can use the numerical data for the maximum intensity (see Sec. III E).

Finally, the points in the central panels in Fig. 2 follow a family pattern $L1-L2=3\mu+\nu$ (not shown) and their spread decreases with the increase of the chiral angle. Tubes with close-to-armchair chirality have very low I_{ii}^m, which tends to zero for chiral angles tending to $\pi/6$. Armchair tubes, however, have maximum intensity that can be comparable to that of zigzag and close-to-zigzag tubes.

In the next sections, we turn to the study of the impact of the effective mass of the transition (Sec. III B), the electron-phonon coupling matrix elements (Sec. III C) and the momentum matrix elements (Sec. III D) on the Raman intensity [see Eq. (8)]. The dependence of these quantities on the tube radius, the chirality, and the transition energy will be discussed in detail.

B. Effective masses

In order to derive the effective masses m_{ii}^* for the optical transitions of the studied nanotubes, we first calculated the imaginary part of the dielectric function and obtained the transition energies E_{ii} as the positions of the peaks of this function. It has to be noted that the πTB model predicts that the optical transitions take place between the maxima of the valence band E_v^m at wave vector k_v and the minima of the conduction band E_c^m at wave vector $k_c \equiv k_v$, because of the symmetry of the valence and conduction bands with respect to the Fermi level. On the other hand, the σ-π band mixing and the structural relaxation in the NTB model lead to a shift between these maxima and minima so that $k_c \neq k_v$. Then, generally, the optical transition takes place at wave vector k_{ii} between k_v and k_c and $E_{ii} \neq E_c^m - E_v^m$ (see Fig. 3). To demonstrate this, we start from the expressions for the valence band E_v and the conduction band E_c in the effective-mass approximation: $E_c^m+\hbar^2(k-k_c)^2/2m_c^*$ and $E_v^m-\hbar^2(k-k_v)^2/2m_v^*$, where m_c^* and m_v^* are the corresponding electron effective masses. We substitute these expressions in the equation $E_{cv}=E_c-E_v=E_{ii}+\hbar^2(k-k_{ii})^2/2m_{ii}^*$ and obtain $k_{ii}=(k_c/m_c^*+k_v/m_v^*)/(1/m_c^*+1/m_v^*)$, i.e., $k_v<k_{ii}<k_c$ or $k_v>k_{ii}>k_c$. This is the case with all armchair and some chiral tubes where the optical transitions take place inside the Brillouin zone. For all zigzag and some chiral tubes, however, $k_{ii}=k_v=k_c=0$.

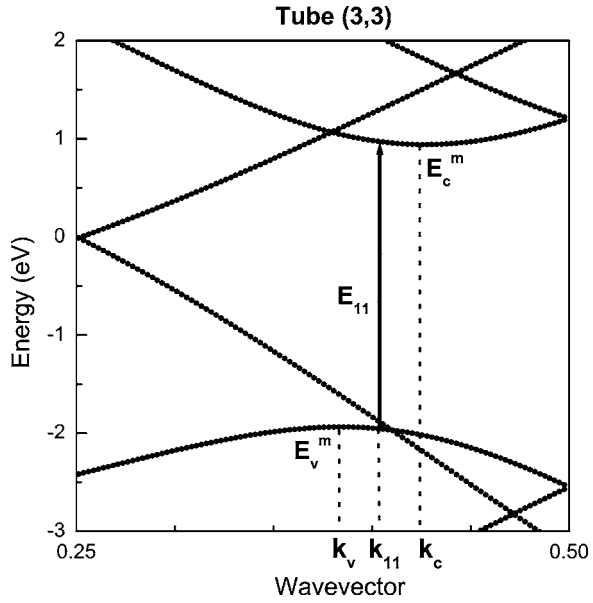

FIG. 3. Part of the band structure of tube (3,3) containing the first optical transition E_{11}. The wave vector is in units $2\pi/T$ (T is the translation period of the tube). The wave vectors k_v, k_{11}, and k_c are equal to 0.386, 0.408, and 0.428, respectively. The energy difference $E_c - E_v$ and the transition energy E_{11} are 2.862 and 2.907, respectively. This figure illustrates the general case of optical transitions in nanotubes when the transition energies are not equal to the vertical separation between extrema of two bands. For the notation, see text.

Substituting k_{ii} in the equation for E_{cv}, one easily arrives at the expressions $1/m_{ii}^* = 1/m_c^* + 1/m_v^*$ and $E_{ii} = E_c^m - E_v^m + \hbar^2(k_c - k_v)^2/2(m_c^* + m_v^*)$. It is clear that the value of the effective mass m_{ii}^* does not depend on the separation between the positions of the band extrema, while the transition energy depends on this shift quadratically.

For the derivation of the effective masses m_{ii}^* from the electronic bands, we used a sampling of 1000 points in the Brillouin zone in order to bracket the k-vector interval, in which the energy separation E_{cv} between two bands with the same quantum number l is close to a given optical transition E_{ii}. Thus we determined the quantum number l_{ii} of the transition E_{ii} and k_{ii} and m_{ii}^* were obtained by a five-point parabolic interpolation in this interval. The variation of E_{cv} with k for a few lowest-energy optical transitions in three tubes with close radii, (4,4), (7,0), and (5,3), is illustrated in Fig. 4.

The obtained effective masses m_{ii}^* are shown versus the tube radius, the chiral angle, and the transition energy in Fig. 5. The effective masses are all smaller than the electron mass in the considered energy range. They increase with the increase of the transition energy and the decrease of the radius and the chiral angle. Zigzag tubes have generally larger masses than the armchair tubes. Similarly to I_{ii}, the effective masses show the same three types of family behavior. Most of the calculated values of m_{ii}^* agree well with the theoretical predictions of the πTB model (see, e.g., Ref. 25). For small radii, some of the NTB effective masses can be up to 1.5 times larger than the πTB ones, but the former converge to the latter with the increase of the radius. The higher effective

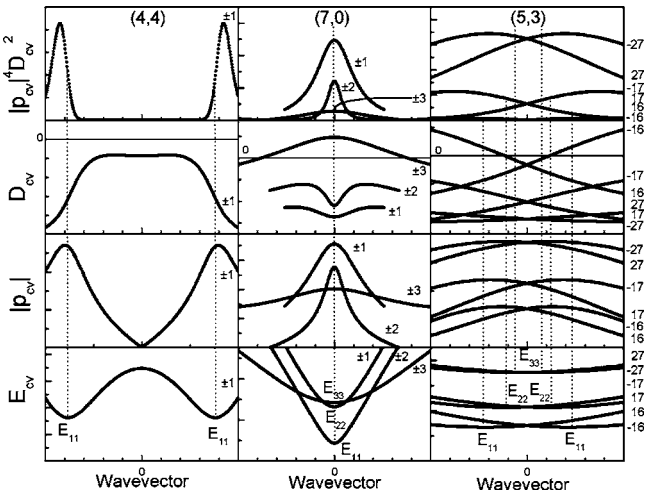

FIG. 4. The calculated k-vector dependence of the interband separation E_{cv}, the momentum and electron-phonon coupling matrix elements, $|p_{cv}|$ and D_{cv}, respectively, and the product $|p_{cv}|^4 D_{cv}^2$ (in arbitrary units) in the entire Brillouin zone for three tubes with close diameters. The quantum numbers l_{ii} of the pairs of conduction and valence bands are shown as well.

masses for small radii in the NTB model originate from the lower and flatter electronic bands than in the πTB model due to the σ-π band mixing. Similarly to the πTB results, the NTB masses exhibit arrangement in strips labeled by the transition index ii (left panels of Fig. 5). The masses for the transitions of the set C_L are larger than for the set C_H. Within each strip, the masses for the zigzag tubes are the largest. For the tubes A, $Z0$, $Z1$, and $Z2$ and for large radii, the effective masses follow the $1/d$ behavior of πTB masses.

The points in the right panels of Fig. 5 have a wedgelike arrangement. The points of set Z_L (set Z_H) lie on the upper (lower) boundary of this region. In the constant-numerator approximation, the strong variation of the maximum intensity $I_{0,ii}^m$ from tube to tube is determined mainly by the effective mass [see Eq. (9)]. Therefore, $I_{0,ii}^m$ is larger for the sets C_L and Z_L than for the sets C_H and Z_H, contrary to the results

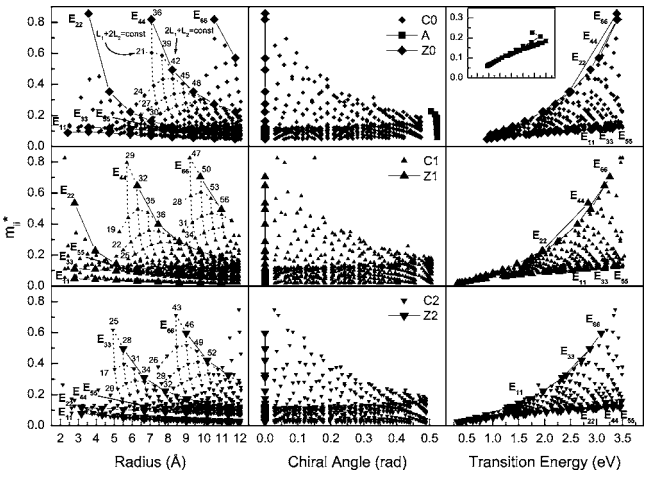

FIG. 5. Same as for Fig. 2 but for the calculated m_{ii}^* (in units of the electron mass).

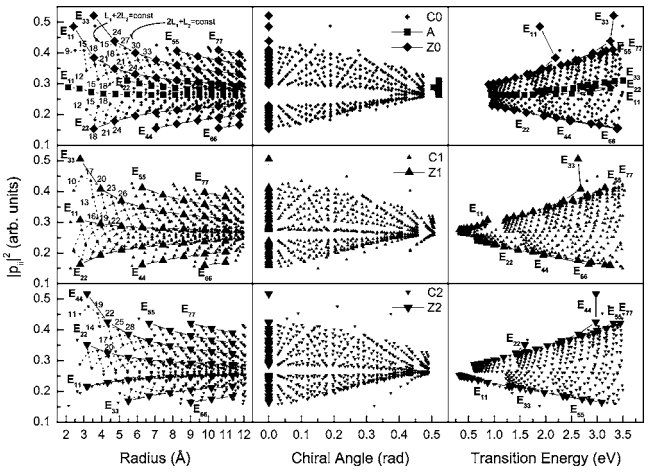

FIG. 6. Same as for Fig. 2 but for the calculated $|p_{ii}|^2$.

of the full calculations for I_{ii}^m from the previous section. At medium transition energies, the ratio of the masses for the sets Z_L, A, and Z_H is approximately 6:3:2 (see right panels of Fig. 5). Bearing in mind that the intensity for armchair tubes generally contains an extra multiplier of 4 in comparison to zigzag and chiral tubes, the ratio of the intensities of the three sets will amount to 6:12:2. Thus, within the constant-numerator approximation and for a given laser energy, the intensity for armchair tubes is predicted to be larger than that for zigzag and chiral tubes. This is not supported by the experimental Raman evidence that chiral tubes have usually as intense Raman lines as those of zigzag and armchair tubes.[18] Therefore, the constant-numerator approximation alone does not yield plausible predictions of the Raman intensity and it is necessary to go beyond this approximation and to account for electron-phonon and electron-photon interactions.

C. Momentum matrix elements

The matrix elements of the momentum p_{ii} are calculated at the transition energies directly by evaluation of the corresponding integrals.[9] The πTB calculations show that p_{ii} is a real quantity and can be positive or negative and has extrema at the points k_{ii}. The sign and the magnitude of p_{ii} versus the radius and the chiral angle can be explained with the distance between k_{ii} and the K point of the Brillouin zone of graphene and the position (inside or outside) relative to the zone boundaries.[26] In the NTB model, p_{ii} has a small imaginary part due to mixing of σ and π states. The absolute value of p_{ii} has similar behavior as in the πTB model. However, the extrema of p_{ii} are slightly shifted with respect to k_{ii} (see Sec. III B). This is illustrated in the case of three tubes with close radii, (4,4), (7,0), and (5,3), in Fig. 4.

In Fig. 6 we show the results for $|p_{ii}|^2$ versus the tube radius, the chiral angle, and the transition energy for all nanotubes as above. The spread of the values of $|p_{ii}|^2$ decreases with the increase of the radius and chirality, and increases with the increase of the transition energy. The points in the three panels follow the same three types of family patterns as for I_{ii}^m. The points in the left panel are situated in strips labeled by the index ii. For the sets C_H, Z_H, and A (C_L and Z_L), $|p_{ii}|^2$ decreases (increases) with the increase of the radius. Within each strip of the set C_H (set C_L), $|p_{ii}|^2$ for zigzag tubes is larger (smaller) than those for chiral tubes with similar radii. For armchair tubes and a given transition ii, $|p_{ii}|^2$ changes only slightly with radius. For a given radius and for ii from 11 to 77, $|p_{ii}|^2$ of zigzag tubes increases in the following order of the indices: 66, 44, 22, 11, 33, 55, and 77 (groups $Z0$ and $Z1$), and 66, 33, 11, 22, 44, 55, and 77 (group $Z2$). The lines of points for armchair tubes are between those with $ii=22$ and 11 for group $Z0$.

It is important to focus on the dependence of $|p_{ii}|^2$ on the transition energy. The points for the various tubes cover a wedgelike region with the points for zigzag tubes lying close to the boundaries and those for armchair tubes occupying the space midway between the two boundaries. The upper boundary contains the points of group Z_H and those of group Z_L are close to the lower boundary. The ratio between the values for groups Z_L, A, and Z_H increases with the increase of the energy. For medium transition energies, the ratio of $|p_{ii}|^4$ for the three groups is about 1:2:3. We can estimate the impact of both the effective mass and the momentum matrix element on the maximum intensity of armchair and zigzag tubes [Eq. (8)] by combining the ratios for both cases and including the extra factor of 4 for armchair tubes to obtain the ratio 6:24:6 (or 1:4:1). This ratio reveals that the maximum intensity of zigzag tubes is four times smaller than for armchair tubes, contrary to the experimental observations of comparable Raman signals. Therefore, the account of the band structure and the electron-photon interactions is not enough for the correct prediction of the Raman intensity and it is necessary to consider the electron-phonon interactions as well.

D. Electron-phonon coupling matrix elements

The electron-phonon coupling matrix elements D_{ii} were calculated at the transition energies using the Hellmann-Feynman theorem for the derivatives of E_{cv} with respect to the atomic coordinates in Eq. (3). The atomic displacements in the RBM were assumed to be strictly radial. As is exemplified in the case of the three tubes with close radii (4,4), (7,0), and (5,3) in Fig. 4, D_{ii} can be positive or negative depending on the tube type and the optical transition. The peculiar change of sign as well as the magnitude can be explained with the closeness of k_{ii} to the K point of graphene and left- and right-situated transitions.[27] However, the sign of the matrix element has no effect on the Raman intensity because the latter depends on D_{ii} to the second power. It is also seen in Fig. 4 that the matrix element D_{cv} as well as the product $|p_{cv}|^4 D_{cv}^2$ is not extremal at k_{ii} with the exception of transitions at the zone center.

The NTB results for D_{ii} for all nanotubes as above are given in Fig. 7 versus the tube radius, the chiral angle, and the transition energy. D_{ii} is negative for the sets C_H (and Z_H) and A and can be positive or negative for the set C_L (and Z_L). The change of the sign and the magnitude of D_{ii} are consistent with recent *ab initio* results.[27] Generally, the absolute value of D_{ii} increases with the increase of the transition en-

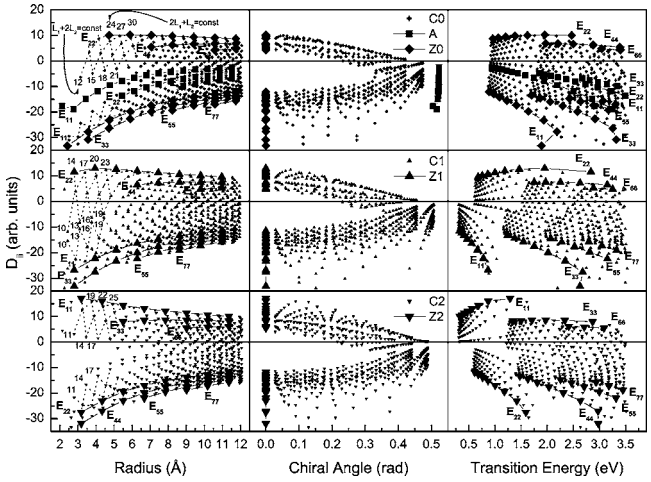

FIG. 7. Same as for Fig. 2 but for the calculated electron-phonon coupling matrix elements D_{ii}.

ergy and with the decrease of the radius. In the limiting case of infinite radius, the breathing motion is just a parallel displacement of the graphene plane with zero frequency. This motion does not change the band structure and has zero Raman intensity. The points for D_{ii} in the left and right panels of Fig. 7 are situated in overlapping strips labeled with the index ii. In each strip, the points have family behavior like that of I_{ii}^m and the absolute values for zigzag tubes are larger than those for chiral tubes with close radii or transition energy.

Again, it is important to estimate the impact of D_{ii} on the maximum Raman intensity. For medium transition energies, the ratio of the absolute value of D_{ii} for sets Z_L, A, and Z_H is about 3:2:6. Remembering that the electron-phonon matrix element enters the intensity to the second power, we see that the overall ratio of the intensities of the three sets, including the factor 4 for armchair tubes, changes to roughly 1:2:4. The transitions of set Z_H have twice higher maximum intensity than armchair tubes, but those of set Z_L have twice less intense lines than for armchair tubes. These results correspond to the experimental observation of comparable Raman scattering cross-sections for zigzag and armchair tubes.

E. Approximate maximum Raman intensity

The approximate maximum Raman intensity $I_{1,ii}^m$ was obtained from Eq. (8) using the values of $|p_{ii}|$, D_{ii}, m_{ii}^*, and F_{ii}^m. The quantity F_{ii}^m depends on the nanotube radius through the frequency of the RBM ω_o. Adopting the simple $1/R$ law for ω_o, it is easy to show that this function increases monotonously with the increase of the radius and changes up to 20% in the considered radius range. Supposing that the nanotube sample consists of tubes with a relatively narrow radius distribution, it is clear that the tube dependence of this function can be ignored. Thus, the strong variation of $I_{1,ii}^m$ from tube to tube will come mainly through the electron-phonon coupling and momentum matrix elements and the effective mass.

The calculated maximum intensity $I_{1,ii}^m$ for all considered nanotubes is similar to that of the full calculation I_{ii}^m plotted

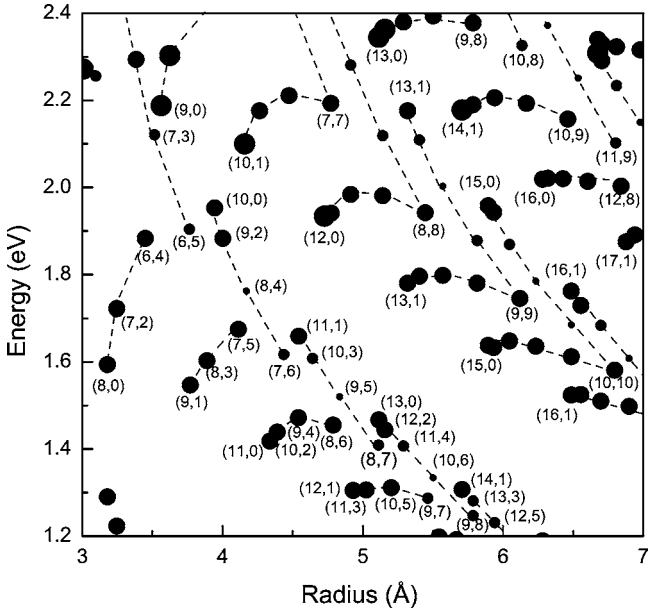

FIG. 8. Energy-radius plot of the maximum Raman intensities $I_{1,ii}^m$ [Eq. (8)]. The intensities are depicted by circles with size corresponding to the logarithm of the intensity. It is clearly seen that for energy E_{22} the intensity of tubes $C2$ and $Z2$ is higher than that of tubes $C1$ and $Z1$, vice versa for energy E_{33}. For metallic tubes, the lower-energy component of the pair (E_{11}, E_{22}) gives rise to higher intensity than the higher-energy one.

in Fig. 2. We chose to present the results for $I_{1,ii}^m$ on an energy-radius plot in Fig. 8 for laser energy and radius ranges corresponding to the Raman data on HiPCO tubes.[18,19] The intensities for different tubes and laser energies are depicted symbolically by circles with different sizes. From Fig. 8, it can be concluded that the intensity for E_{22} is much higher for tubes $C2$ and $Z2$ than for $C1$ and $Z1$, but for E_{33} it is vice versa.[18] For metallic tubes, the lower-energy component of the pair (E_{11}, E_{22}) has higher intensity than the lower-energy one (see also Fig. 1) in agreement with recent Raman measurements on HiPCO samples.[17,18]

The comparison of the numerical data for the approximate intensities with the data for the exact ones shows that $I_{1,ii}^m$ underestimates I_{ii}^m up to about 5% for the most intense features in the RRP and up to 50% for the weakest ones. The origin of this disagreement can be sought in the approximations made in the derivation of $I_{1,ii}^m$. First, it was assumed that the features in the RRPs are nonoverlapping, which is not entirely justified for separations smaller than about 0.5 eV. Second, the matrix elements in the same equation were assumed to be slightly k dependent and were pulled out of the sum at the point of the optical transition. The remaining sum was calculated analytically using the effective-mass approximation. In the case of two close features at energies E_{aa} and E_{bb}, the inaccuracy due to the first assumption can be decreased by replacing the terms $A' I_{1,aa}^m |F_{aa}/F_{aa}^m|^2 + A' I_{1,bb}^m |F_{bb}/F_{bb}^m|^2$ in the expression of the RRP by $A' |s_{aa}\sqrt{I_{1,aa}^m} F_{aa}/F_{aa}^m + s_{bb}\sqrt{I_{1,bb}^m} F_{bb}/F_{bb}^m|^2$ (s_{ii} is the sign of D_{ii}). The disagreement due to the second approximation can be reduced if the product $|p_{cv}|^2 D_{cv}$ and E_{cv} are expanded in

series of $k-k_{ii}$ up to higher powers in the vicinity of each optical transition. Since the NTB model has a certain degree of inaccuracy relative to the *ab initio* approach, we did not attempt to improve the approximate result $I^m_{1,ii}$ [Eq. (8)].

On the other hand, there are difficulties in the derivation of I^m_{ii} of close features of the RRP. Normally, this should be done by fitting a sum of independent peaks to the calculated Raman profile. Unfortunately, the function $|F_{ii}|^2$ was derived using certain approximations and does not describe well the shape of the low-intensity features of the RRP. Additionally, the error of such fitting can be very large for very close peaks with peak intensities differing by several orders of magnitude. Note that such a problem does not arise for the first and second optical transitions in semiconducting tubes.[23] Bearing in mind these crucial problems in the derivation of I^m_{ii} for low-intensity and close peaks of the RRP, we assume that the data for $I^m_{1,ii}$ (Ref. 28) are more appropriate for simulation of the Raman spectrum of nanotubes in the RBM region. In this case, the resonance Raman profile for a given tube is given by the expression

$$I(E_L,\omega_o) = A' \sum_{ii} I^m_{1,ii} \left| \frac{F_{ii}}{F^m_{ii}} \right|^2, \tag{11}$$

where the summation is over the optical transitions of the tube. The total Raman intensity of a nanotube sample at a given laser energy versus Raman shift ω can be simulated using the formula

$$I_{tot}(E_L,\omega) = \sum g I(E_L,\omega_o) \frac{1}{(\omega-\omega_o)^2+\gamma_o^2}. \tag{12}$$

Here g is the distribution function of the tubes in the sample, γ_o is the phonon linewidth, and the summation is carried out over all tube types. The results of the simulation of several Raman spectra for a given tube distribution are shown in comparison with experimental ones in Ref. 23. In the case of unknown tube distribution, the distribution function can be determined by fitting Eq. (12) to measured Raman spectra at several laser energies.

F. Maximum Raman intensity and absorption coefficient

In order to compare the conditions for observation of the nanotubes in Raman and optical absorption spectroscopies, we also calculated the maximum absorption coefficient. In Fig. 9, $\alpha^m_{1,ii}$ evaluated from Eq. (10) is shown versus the tube radius, the chiral angle, and the transition energy. It is clear the $\alpha^m_{1,ii}$ changes only up to three times in the considered radius and energy range. The points in the plots in the left panels show striplike arrangement for transitions with different indices ii. Generally, the values of $\alpha^m_{1,ii}$ in the strips decrease with the increase of ii for tubes with close radii or

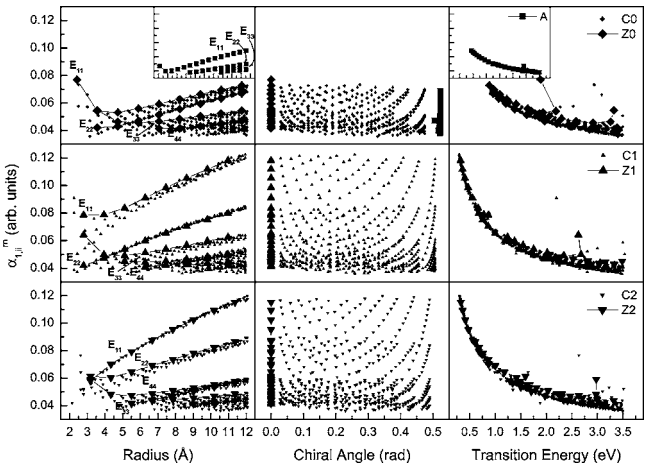

FIG. 9. Same as for Fig. 2 but for the maximum absorption coefficient $\alpha^m_{1,ii}$.

transition energies. For large radii, $\alpha^m_{1,ii}$ is roughly proportional to the radius, which is corroborated by the result of the πTB model.[26] The central panels show that there is no evident correlation between the absorption coefficient and the chiral angle of the tubes. In the right panels, all points of $\alpha^m_{1,ii}$ lie on a very narrow strip that follows roughly the power law $1/\sqrt{E_{ii}}$. While the maximum absorption coefficients of different tubes differ as much as three times, the maximum Raman intensity of the various tubes varies over five orders of magnitude. Additionally, some tubes will have negligible scattering cross section for all laser energies up to 3.5 eV. These circumstances can make difficult the structural characterization of nanotube samples using Raman spectroscopy.

IV. CONCLUSIONS

In conclusion, we calculated the resonance Raman profiles of the radial-breathing mode for all 300 SWNTs in the radius range from 2 Å to 12 Å and for all transition energies up to 3.5 eV within a symmetry-adapted nonorthogonal tight-binding model. The calculated maximum Raman intensity is largest for tubes with close-to-zigzag chirality as well as for some armchair tubes. The maximum intensity for transitions 11, 33,55,77,… in zigzag tubes $Z0$ and $Z1$, and transitions 22,44,55, 77, … in zigzag tubes $Z2$ is higher than for the rest of the transitions in zigzag tubes.

For the analysis of the effect of the electron-phonon and electron-photon interactions on the Raman intensity, we approximated the expression for the maximum intensity with the product of the momentum matrix element to the fourth power, the electron-phonon coupling matrix element to the second power, and the effective mass, all of them calculated at the optical transitions. We showed that the assumption for tube-independent matrix elements yields a totally different behavior of the maximum intensity than the result of the full calculation. Accounting for the electron-phonon and electron-photon interactions allowed us to reach an agreement with the experimentally observed behavior of the intensity (see Ref. 23).

The comparison of the conditions for observation of nanotubes by Raman and optical absorption spectroscopies reveals that, while all nanotubes have comparable maximum absorption coefficients, their maximum Raman intensity can vary from very low to very high from tube to tube. Therefore, Raman data collected at several laser energies have to be used for the unambiguous determination of the tube distribution characterization by means of the theoretical maximum Raman intensities.

ACKNOWLEDGMENTS

V.N.P. was supported financially by a Marie-Curie Program (MEIF-CT-2003-501080). L.H. was supported by the Belgian National Fund (FNRS). This work was partly funded by the Belgian Interuniversity Research Project on quantum size effects in nanostructured materials (PAI-IUAP P5/1). V.N.P., L.H., and Ph.L. were partly supported by the NATO CLG 980422.

*Corresponding author. Permanent address: Faculty of Physics, University of Sofia, BG-1164 Sofia, Bulgaria.

[1] *Carbon nanotubes: Synthesis, Structure, Properties, and Applications*, edited by M. S. Dresselhaus, G. Dresselhaus, and Ph. Avouris (Springer-Verlag, Berlin, 2001).

[2] R. Saito, T. Takeya, T. Kimura, G. Dresselhaus, and M. S. Dresselhaus, Phys. Rev. B **57**, 4145 (1998).

[3] V. N. Popov, V. E. Van Doren, and M. Balkanski, Phys. Rev. B **59**, 8355 (1999).

[4] J. Kürti, G. Kresse, and H. Kuzmany, Phys. Rev. B **58**, R8869 (1998).

[5] D. Sánchez-Portal, E. Artacho, J. M. Soler, A. Rubio, and P. Ordejón, Phys. Rev. B **59**, 12678 (1999).

[6] L. Henrard, V. N. Popov, and A. Rubio, Phys. Rev. B **64**, 205403 (2001).

[7] V. N. Popov and L. Henrard, Phys. Rev. B **65**, 235415 (2002).

[8] R. Saito, G. Dresselhaus, and M. S. Dresselhaus, *Physical Properties of Carbon Nanotubes* (Imperial College Press, London, 1998).

[9] V. N. Popov, New J. Phys. **6**, 17 (2004).

[10] V. N. Popov and L. Henrard, Phys. Rev. B **70**, 115407 (2004).

[11] S. Reich, C. Thomsen, and P. Ordejón, Phys. Rev. B **65**, 155411 (2002).

[12] C. D. Spataru, S. Ismail-Beigi, L. X. Benedict, and S. G. Louie, Phys. Rev. Lett. **92**, 077402 (2004).

[13] C. L. Kane and E. J. Mele, Phys. Rev. Lett. **93**, 197402 (2004).

[14] S. M. Bachilo, M. S. Strano, C. Kittrell, R. H. Hauge, R. E. Smalley, and R. B. Weisman, Science **298**, 2361 (2002).

[15] R. B. Weisman and S. M. Bachilo, Nano Lett. **3**, 1235 (2003).

[16] S. K. Doorn, D. A. Heller, P. W. Barone, M. L. Usrey, and M. S. Strano, Appl. Phys. A **78**, 1147 (2004).

[17] C. Fantini, A. Jorio, M. Souza, M. S. Strano, M. S. Dresselhaus, and M. A. Pimenta, Phys. Rev. Lett. **93**, 147406 (2004).

[18] H. Telg, J. Maultzsch, S. Reich, F. Hennrich, and C. Thomsen, Phys. Rev. Lett. **93**, 177401 (2004).

[19] P. M. Rafailov, H. Jantoljak, and C. Thomsen, Phys. Rev. B **61**, 16179 (2000).

[20] A. Jorio, A. G. Souza Filho, G. Dresselhaus, M. S. Dresselhaus, R. Saito, J. H. Hafner, C. M. Lieber, F. M. Matinaga, M. S. S. Dantas, and M. A. Pimenta, Phys. Rev. B **63**, 245416 (2001).

[21] E. Richter and K. R. Subbaswamy, Phys. Rev. Lett. **79**, 2738 (1997).

[22] M. Canonico, G. B. Adams, C. Poweleit, J. Menendez, J. B. Page, G. Harris, H. P. van der Meulen, J. M. Calleja, and J. Rubio, Phys. Rev. B **65**, 201402(R) (2002).

[23] V. N. Popov, L. Henrard, and Ph. Lambin, Nano Lett. **4**, 1795 (2004).

[24] R. Loudon, Proc. R. Soc. London **275**, 218 (1963).

[25] T. G. Pedersen, Phys. Rev. B **67**, 073401 (2003).

[26] J. Jiang, R. Saito, A. Grüneis, G. Dresselhaus, and M. S. Dresselhaus, Carbon **42**, 3169 (2004).

[27] M. Machón, S. Reich, H. Telg, J. Maultzsch, P. Ordejón, and C. Thomsen, Phys. Rev. B **71**, 035416 (2005).

[28] See EPAPS Document No. E-PRBMDO-72-024527 for the table containing the values of the radius and chiral angle of the relaxed nanotube structure, k_{ii}, l_{ii}, E_{ii}, m^*_{ii}, $|p_{ii}|^2$, D_{ii}, and $I^m_{1,ii}$ for all 300 single-walled carbon nanotubes in the radius range from 2 Å to 12 Å and for transition energies up to 3.5 eV. This document can be reached via a direct link in the online article's HTML reference section or via the EPAPS homepage (http://www.aip.org/pubservs/epaps.html).